JGR Solid Earth

RESEARCH ARTICLE
10.1029/2018JB015844

Key Points:
- What kind of physical process could produce ground short-term bradyseismic oscillation in calderas unrest?
- Linear time invariant approximation applied to multiphase thermo-fluid dynamical evolution of the Campi Flegrei hydrothermal system
- Short-term deformation source parameters estimated by Green's function-based inversion of the ground deformation at Campi Flegrei caldera

Supporting Information:
- Supporting Information S1
- Data Set S1
- Data Set S2
- Figure S1

Correspondence to:
Z. Petrillo,
zaccaria.petrillo@ov.ingv.it

Citation:
Petrillo, Z., D'Auria, L., Mangiacapra, A., Chiodini, G., Caliro, S., & Scippacercola, S. (2019). A perturbative approach for modeling short-term fluid-driven ground deformation episodes on volcanoes: A case study in the Campi Flegrei caldera (Italy). *Journal of Geophysical Research: Solid Earth*, *124*, 1036–1056. https://doi.org/10.1029/2018JB015844

Received 27 MAR 2018
Accepted 23 DEC 2018
Accepted article online 29 DEC 2018
Published online 26 JAN 2019

A Perturbative Approach for Modeling Short-Term Fluid-Driven Ground Deformation Episodes on Volcanoes: A Case Study in the Campi Flegrei Caldera (Italy)

Z. Petrillo[1], L. D'Auria[2], A. Mangiacapra[1], G. Chiodini[3], S. Caliro[1], and S. Scippacercola[1,4]

[1]Istituto Nazionale di Geofisica e Vulcanologia, Osservatorio Vesuviano, Naples, Italy, [2]Instituto Volcanológico de Canarias, San Cristóbal de La Laguna, Spain, [3]Istituto Nazionale di Geofisica e Vulcanologia, sezione di Bologna, Bologna, Italy, [4]Dipartimento di Economia, Management, Istituzioni, Università degli Studi di Napoli "Federico II", Naples, Italy

Abstract Ground deformation in volcanic areas is linked to various, often interconnected processes such as magma intrusion, pressurized fluid migration, and thermal expansion effects. The presence of active and extended hydrothermal systems plays a key role and affects the deformation phenomenon in complex ways. In this study, we propose a generalized conceptual and mathematical model, which allows retrieving the flow rate of fluid injection in a volcanic hydrothermal system, assuming a ground deformation data set as input. The basic assumption is that short-term ground uplift episodes (with characteristic periods of less than 5 years) depend on the injection of volcanic fluids into the hydrothermal system. Then, assuming a deformation field shape independent of time and a linear time-invariant relation between the amount of injected fluid and the resulting ground deformation, we define a Green's function as the product of spatial and temporal components. The case study is a 3-D elastic model with permeability and porosity for the Campi Flegrei caldera, Italy. By Green's function, a 2-km-long source at 2.4-km depth, which matches the interferometric synthetic aperture radar deformation, is localized and the amount of injected volcanic fluid in the last 20 years of high-frequency deformation episodes estimated. In conclusion, we find a good agreement between the measured and estimated temporal deformation patterns and, principally, that fluid injection rates can be retrieved from the deformation field at volcanoes.

1. Introduction

This work concerns the short-term transient deformations related to fluid injection episodes in hydrothermal systems.

As a test case, we refer to the Campi Flegrei caldera (CFc) and particularly to the high-frequency deformation episodes. Chiodini et al. (2003, 2012) and Chiodini (2009) showed the correlation between these episodes and the variations in the amounts of gas species measured in the Solfatara crater.

The CFc is a broad (90 km^2) and densely populated (~1,500,000 inhabitants; Orsi et al., 2004, 2009) caldera in southern Italy characterized by a very high volcanic risk (Chiodini et al., 2015, 2016; D'Auria et al., 2015; Zollo et al., 2008).

The CFc is an active volcanic and geothermal area where volcanism has been documented since 60 ka bp (Pappalardo et al., 1999). Two major volcanic events mark the history of this area: the Campanian Ignimbrite eruption (39 ka; De Vivo et al., 2001), which led to the deposition of approximately 150 km^3 (DRE) of pyroclastic deposits across an area of 30,000 km^2, and the Neapolitan Yellow Tuff eruption (15 ka; Deino et al., 2004), which covered 1,000 km^2 with approximately 40 km^3 (DRE) of pyroclastic deposits (Barberi et al., 1978; Orsi et al., 1995; Rosi & Sbrana, 1987). In the last 15 ka, the eruptive vents (Di Renzo et al., 2011) have been located within the caldera, which has always been the site of intense volcano-tectonic activity and hosts a high-temperature geothermal field characterized by CO_2-rich fumaroles and thermal springs (Caliro et al., 2007; Chiodini, 2009; Chiodini et al., 2001, 2015). In particular, bradyseismic episodes still affect the caldera floor, generating uplift and inflation events (Del Gaudio et al., 2010, and references

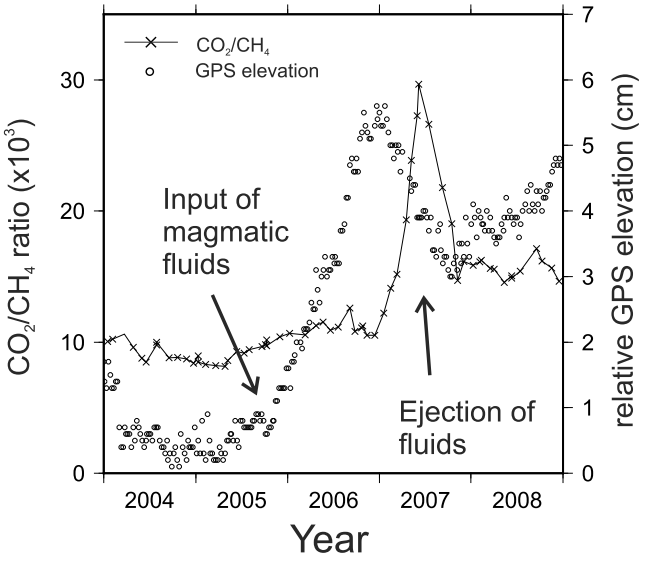

Figure 1. Chronograms of CO_2/CH_4 ratios and ground elevations during the 2006 uplift (Chiodini, 2009).

therein; Barberi et al., 1984; Casertano et al., 1977; Corrado et al., 1977; Morhange et al., 2006; Orsi et al., 1999; Parascandola, 1947; Trasatti & Bonafede, 2008).

The ground deformation data set adopted consists of optical leveling, continuous Global Positioning System (GPS), and interferometric synthetic aperture radar (SAR) measurements. Furthermore, as additional constraint, we used the geochemical data from CO_2 and H_2O fluxes discharged by the main fumaroles of the CFc. One of the most impressive manifestations of the volcanic activity is the deformation of the volcanic edifice.

An important role in the ground deformation of calderas is played by the hydrothermal system. Maurizio Bonafede (1991) made the first attempt to give a quantitative description of the impressive 1982 uplift episode at the CFc based on the role of fluids in volcanic crises. In this paper, the thermoelastic expansion of the geothermal system due to heating effects explains the deformation of a relative superficial source. In De Natale et al. (2006), a mixed magmatic-geothermal source is adopted to explain the bradyseism mechanism. In this model, the geothermal system delays the maximum uplift after the magma injection and accounts for the slow deflation rate, on the basis of the pressure discharged by the permeability mechanism. The role of the pressurization of the hydrothermal system has been recently underlined by several authors (Fournier & Chardot, 2012; Hutnak et al., 2009; Rinaldi et al., 2010); poroelasticity links transient pressure changes and short-term deformation. Long-term deformation, instead, should be mostly related to the thermoelastic effects due to a sustained injection of hot fluid at depth (Chiodini et al., 2015; Fournier & Chardot, 2012).

In the last 25 years, the ground deformation pattern at the CFc has consisted of long-term deflation-inflation (with a reversal trend since 2005) and short-term uplift episodes with durations of a few years (Chiodini et al., 2012; D'Auria et al., 2011).

For the CFc, various models of ground deformation have been proposed for the period 1987–2013 (Amoruso et al., 2014; Battaglia et al., 2006), and both hydrothermal (D'Auria et al., 2012) and magmatic sources have been proposed (Amoruso et al., 2014; 2014; D'Auria et al., 2015; Trasatti et al., 2015). In particular, D'Auria et al. (2012), using an advanced imaging method, have shown that the short-term deformations during the 2000 and 2006 ground uplift episodes were related to the upward migration of fluid batches.

Geochemical data support hydrothermal origins for most of the ground deformation episodes (Chiodini et al., 2010, 2012, 2015). As shown in Chiodini (2009), the strong correlation between ground deformation measured at the center of the caldera and the variation in the CO_2/CH_4 ratio (Figure 1) measured in the Solfatara crater suggests a causal physical link between fluid injection and unrest episodes. Furthermore, Chiodini et al. (2015) have demonstrated that a strong correlation exists between geochemical and ground deformation time series. In particular, in Chiodini et al. (2012) it is discussed how the degassing episodes trigger short-term deformation episodes. On the basis of this correlation, our intent is to quantitatively link degassing episodes to the deformation, in order to interpret with a physical unitary model the entire 1992–2015 short-term deformation pattern.

In our study, the primary intent is to develop a general methodology to recover time-varying fluid injection rates in hydrothermal systems, starting from the observed short-term ground deformation. To achieve our goal, we have used a linearized approach to define a Green's function able to estimate the amount of injected fluids.

We have used the TOUGH2 code (Pruess, 2004) to model the dynamics of the hydrothermal system. We take into account the structural complexity of the volcano by using the 3-D permeability and porosity model for the CFc proposed in Petrillo et al. (2013), which also considers the bathymetry and water table topography (Figure 2). The use of a correct permeable-porous model is crucial to estimate the correct Green's function. In Appendix A, the strong dependence of the function on the permeability and porosity variations is shown.

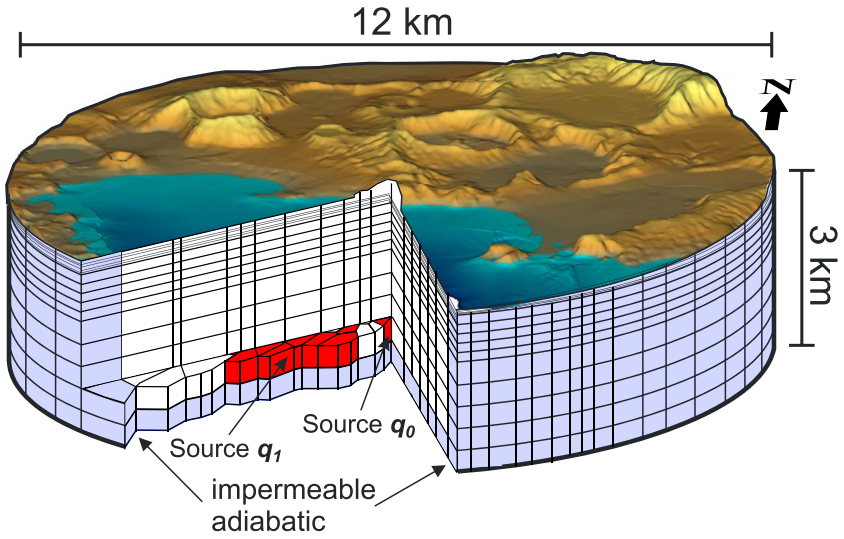

Figure 2. Computational domain of the Campi Flegrei caldera 3-D model. The Solfatara crater is located at the center of the domain. The stationary fluid source ($\mathbf{q_0}$) and the source of transient fluid injections ($\mathbf{q_1}$) are indicated in the figure. The topography shown in the figure is only indicative and is not included in the computational domain, which is also indicated (modified from Petrillo et al. 2013).

The method applied in the present work relies on a perturbative approach to the thermo-fluid dynamic state, which allows us to easily model time-limited transients, perturbing the steady state.

In section 2, we discuss the thermo-fluid dynamical model and our heuristic approach leading to the linear approximation. In section 3, we discuss the numerical approach to determine the optimal shape and location of the fluid injection source and the computation of the temporal Green's functions, while in section 4, we illustrate how these functions are used within the adopted inverse method. The application of this method to the CFc data set and its results are illustrated in section 5 and discussed in section 6. Appendix A shows the results of synthetic numerical test cases performed with varying permeability ($[10^{-12}\ 10^{-16}]$ m^2) and porosity (10, 40%) in a 3-D domain. We demonstrate and analyze the dependency of Green's function on the two physical parameters. The last section of Appendix A shows the constancy of the deformation pattern with respect to time for different permeability model.

2. Linearized Approach: Theoretical Basis

2.1. Linearization Hypothesis

We consider the thermo-fluid dynamics equation system for multiphase flow in porous media (Pruess, 2004). The mass and energy balance equation can be written in differential form as

$$\frac{\partial M^k}{\partial t} = -\nabla \cdot F^k + q^k, \quad k = 1, ..., N+1 \tag{1}$$

where M^k is the term that accounts for both the mass accumulation, as the index k spans the interval [1, N] (N representing the number of components, in our case, 2: H_2O and CO_2) and the energy stored as heat when $k = N + 1$. F^k represents equivalently mass or heat flux as the former term does, and q^k is the source term.

The mass accumulation term can be written as a sum over all the fluid phases β:

$$M^k = \varphi \sum_\beta S_\beta \rho_\beta X_\beta^k \tag{2}$$

where φ is the rock porosity, S_β is the fraction of pore volume occupied by phase β, ρ_β is the phase density, and X_β^k is the mass fraction of component k present in phase β.

The heat accumulation term in a multiphase system is

$$M^{N+1} = (1-\varphi)\rho_R C_R T + \varphi \sum_\beta S_\beta \rho_\beta u_\beta \tag{3}$$

where ρ_R *is* the solid matrix density and C_R its specific heat, T is temperature, and u_β is the specific internal energy in phase β. In general, the temperature associated with phase β is not the same as the matrix temperature, but in general, in hydrothermal system, with very low values for advective terms, there is local thermal equilibrium, and the temperatures of the two terms of (3) are the same.

The second term in equation (1) (advective term) is governed by the multiphase Darcy law:

$$\boldsymbol{F}_\beta = -k \frac{k_{r\beta}\rho_\beta}{\mu_\beta(T)} \left(\nabla P_\beta - \rho_\beta \boldsymbol{g}\right) \tag{4}$$

where $\boldsymbol{F}_\beta$ represents the mass flux in phase β, k is the absolute permeability, $k_{r\beta}$ is the relative permeability of phase β, and $\mu_\beta(T)$ is the viscosity of phase β as a function of temperature.

The nonlinearity arises from the presence of the advective term ($-\nabla \cdot F^k$) in equation (1) and from the state equation for the fluid phases. If we perturb a stationary fluid flow pattern (i.e., by injecting a batch of fluids), exchanges of heat between the rock matrix and the fluids and phase changes (with the release or absorption of heat) can occur. The processes are generally nonlinear affecting, for instance, the viscosity $\mu_\beta(T)$ and consequently the mass flux term $\boldsymbol{F}_\beta$ in the Darcy relation (equation (4)).

Our hypothesis is that during injection episodes of short duration, nonlinear effects are negligible, which means, for instance, that $\mu_\beta(T)$ does not change significantly with temperature and that phase changes do not appreciably affect the pressure of the entire domain. These hypotheses have been positively tested and verified numerically (see section 3).

A similar effect has been shown by Hutnak et al. (2009) and Fournier and Chardot (2012). These studies proved that for a limited time period (approximately years in our case) and depending on the considered domain, the pressure is linearly correlated with the fluid injection rates.

2.2. Derivation of Green's Function

We define the source term for achieving stationary conditions (i.e., stationary fluid injection beneath Solfatara) as $q_o^k(\mathbf{x})$ (see Petrillo et al., 2013, for details). Hence, for steady state conditions, equation (1) reduces to

$$\nabla \cdot F_0^k = q_0^k(\boldsymbol{x}) \tag{5}$$

The complex structure of the convective cells, discussed in Petrillo et al. (2013), is characterized by very low fluid velocities (on the order of 10^{-4} m/s). Let us consider now the solution for equation (1) resulting from a perturbed source term:

$$q^k(\mathbf{x}, t) = q_0^k(\mathbf{x_0}) + q_1^k(\mathbf{x}, \tau) \tag{6}$$

where $q_1^k(\mathbf{x}, \tau)$ is the spatiotemporal source pattern, which is different from 0 only within the source region and during an injection.

We now write any thermodynamic quantity θ^i in the perturbed solution of equation (1) as $\theta^i = \theta_0^i + \epsilon\theta_1^i \theta^i = \theta_0^1 + \epsilon\theta_1^i$, where θ_0^i is the value of the quantity in the stationary solution of equation (5) and $\epsilon\theta_1^i$ represents the perturbation of the same quantity. Replacing this quantity in equation (1), then subtracting equation (5) and retaining only the terms in $\in$, we obtain a linearized equation system for the perturbed quantities that can be written as

$$L^k\left(\theta_i^1(\boldsymbol{x}, t)\right) = q_1^k(\boldsymbol{x}_1, \tau) \tag{7}$$

where L_k are linear differential operators. We can then separate the spatial and temporal contributions to the source term:

$$q_1^k(\boldsymbol{x}_1, t) = q_1^k(x)s(t) \tag{8}$$

where $q_1^k(x)$ is the spatial source pattern and $s(t)$ is the injection rate. If we set $s(t) = \delta(t)$ in equation (7), its solution represents a Green's function, which allows us to write any solution for equation (7) as a convolution integral:

$$\theta_i^1(\boldsymbol{x}, \mathrm{t}) = \int_V d\boldsymbol{x}_1 q_1^k(\boldsymbol{x}_1) \int_{-\infty}^{\infty} G_i(\boldsymbol{x}_1, \tau; \boldsymbol{x}, t)s(\tau)\, d\tau \tag{9}$$

In practice, we do not directly observe the thermodynamic quantities θ_i^1 but rather the ground deformation parameters ψ_n, which are merely linear functionals of θ_i^1 in an integral form such as:

$$\psi_n(t) = \sum_i \int_V \Psi^i \left[\theta_i^1(t)\right] dV \tag{10}$$

Note that now the integral volume in equation (10) is extended to the whole space, while in equation (9), it refers to the source of the thermodynamic problem (q_1 in Figure 2); Ψ^i is the contribution to the z-deformation calculated with COMSOL, which connects, for example, the pressure of one volume element $\left(\theta_{\mathrm{pres}}^1(x, y, z)\right)$ in the integral in equation (10) at a generic point on Earth's surface. In this work, we model the ground deformation considering both the poroelastic and the thermoelastic effects (Rinaldi et al., 2010; Vasco et al., 2002). In the following sections, we show how once $q_1^k(x)$ has been determined, $s(t)$ can be deconvolved from the time series of ground deformation parameters $\psi_n(t)$.

3. Numerical Computation of Green's Function

In this section, we discuss the forward part of our method separating the three principal logic blocks into paragraphs. We use the forward approach to reproduce deformation data and show the validation of the linear approximation, as regard the response of the system to impulses of different amplitude.

The first block computes the pressure and temperature fields (TOUGH2) as functions of time. The second block calculates (COMSOL) the associated deformation field and is used to define the source localization and its extent. The third block is used to define the temporal structure of Green's function associated with the deformation source.

3.1. Thermo-fluid Dynamical Model

In this work, we used the geothermal simulator TOUGH2 (Pruess, 1991, 2004), which can model nonisothermal flows of multicomponent (water and carbon dioxide) and multiphase (gas and liquid) fluids in porous and fractured media. Details about the code can be found in Sutton and Mc Nubb (1977), Pruess (1987, 1991), and Moridis and Pruess (1998).

Previous models by Todesco et al. (2003, 2004), Todesco and Berrino (2005), and Todesco (2009) represent the first attempt to support compatibility between hydrothermal fluids injections in CFc and the resultant deformation field. They found that the estimated amount of fluids needed to obtain such a deformation extent is compatible with the measured amount of gas collected at the surface and that the estimated gravity changes are compatible with the phase variation of the gas involved in the hydrothermal system. However, their results give no constraints on the location and the extent of the deformation source and there is no evaluation on the misfit between the calculated and the measured deformation patterns. In particular, in Todesco (2009) it is stated the relevance of the source size, the fluid injection rate, and the duration of the unrest periods for unrest characterisation, that is what we have numerically calculated with our model for the CFc volcanic system.

To model the spatial and temporal ground deformation pattern of the CF caldera caused by the injection of fluid batches at depth, we used the steady state flow determined by Petrillo et al. (2013) as a background pattern for the CFc. This model allowed calculating the pressure and temperature in the steady state for the whole CFc model. We neglected the changes in the porosity and permeability due to pressure and temperature variations, since it has already been shown that these effects are generally negligible (Fournier & Chardot, 2012; Hurwitz et al., 2007; Hutnak et al., 2009). The substantial difference between

the new model and the ones in Petrillo et al. (2013) is the presence of a new extended source. This new source is not represented as a point because, in order to match the deformation data, it must have a finite extent.

In section 3.2 we will show how this source is constrained by a length of 2 km. Although this source leaves the structure of the convective cells unchanged (Figure 6), it completely modifies the deformation field. The computed deformation pattern matches the interferometric SAR data and contemporaneously allows most of the gas flow to reach the surface around the Solfatara crater.

The computational domain for the CFc consists of a cylinder 3,000 m high and 12,000 m in diameter saturated with water and CO_2 and divided into 11,880 variable-sized elements with a finer discretization toward the top of the domain (Figure 2). We also consider the topography of the water table onshore and the bathymetry offshore.

The bottom cells are assigned a permeability approximately 2 orders of magnitude lower than that of the overlying strata and a temperature fixed at 320 °C. The top boundary surfaces, both onshore and offshore, are fixed at specific pressure and temperature conditions and open to the flow of heat and fluids. The temperature of the top is fixed at the average value for the area (20 °C), while the pressure is assumed to be 1.013 bar.

The model is initially saturated by liquid water with low CO_2 contents. In the entire domain, the initial total pressure conditions have been assigned to increase linearly with depth following the hydrostatic gradient. Initial temperatures are set according to an averaged linear thermal gradient of 0.105 °C/m on the basis of the geothermal wells drilled in the CF (AGIP, 1987). Quasi-steady state conditions are achieved by injecting 67 kg/s of a hot (350 °C) mixture of CO_2 and H_2O at a depth of approximately 2,400 m beneath the Solfatara crater for 4,000 years. The very low permeability of the layers underlying the injection cell prevents the downward expansion of the injected fluids. The selected injection rate (67 kg/s of a CO_2 and H_2O mixture) approximately matches the CO_2 flux measured in the Solfatara area (17 kg/s, Chiodini et al., 2011). Furthermore, the gas mixture has a CO_2/H_2O weight ratio of approximately 0.34 (Chiodini et al., 2012).

The numerical computation of Green's function is done by injecting a batch of fluids at a rate of 4,000 kg/s for 15 days along with the background source beneath Solfatara.

We computed pressure and temperature variations (relative to the steady state) in the hydrothermal system during fluid injection episodes by using the outputs of the TOUGH2 code. These quantities (i.e., the θ_i^1 in equation (10)) were then used to compute the corresponding poroelastic and thermoelastic strains (Rinaldi et al., 2010; Vasco et al., 2002). Finally, using the finite element software COMSOL-Multiphysics, we computed spatial and temporal ground deformation patterns related to transient perturbations in the hydrothermal system. This last numerical step, in practice, performs the integration required by equation (10).

To perform the quasi-static elastic modeling, we used a computational volume with a radius of 20 km and a depth of 20 km. The top surface has been modeled following the topography of the CFc area. The elastic properties are spatially variable and defined following recently published 3-D tomographic models (D'Auria et al., 2008). The source terms, taking into account both thermoelastic and poroelastic strains, are defined to be spatially variable, and they follow the scalar field of the pressure and the temperature resulting from the TOUGH2 simulations. The source terms are allowed only within a cylindrical volume with a radius of 4 km and a high of 4 km, outside that cylinder the source terms are null.

3.2. Determination of the Source Shape and Depth

We assume that during a short-term uplift phase, the deformation pattern remains essentially unchanged (Figures A3–A7). This situation is confirmed by various recent studies on the ground deformation source at Campi Flegrei (Amoruso et al., 2014; Amoruso et al., 2014; D'Auria et al., 2015). This observation justifies the choice of holding the term $q_1^k(\mathbf{x_1})$ in equation (8) constant.

To correctly define the shape and depth of the source of these injections (i.e., the cell elements of the function $q_1(\mathbf{x_1})$), we used an exhaustive grid-search exploration of a subspace, constrained between 2 and 3 km of depth, with a radius of 4 km centered in Pozzuoli city (center of maximum uplift). Each model consists of a set of adjacent cells aligned along a straight line, which occupies the 3-D space of the discretization grid.

We tested all the possible combinations by considering the straight lines connecting all the possible couples of cell centers.

We explored the entire model space and defined a misfit function by comparing the synthetic ground deformation pattern to the observed one. Applying equations (9) and (10) to simulate a temporal Green's function and setting $s(t) = \delta(t)$,

$$\theta_i(\boldsymbol{x}, \mathrm{t}) = \int_V q_1^k(\boldsymbol{x}_1) G_i(\boldsymbol{x}_1, 0; \boldsymbol{x}, t) d\boldsymbol{x}_1 \tag{11}$$

we compared the synthetic ground deformation at the peak of the injection (i.e., after 15 days) with the actual ground deformations measured by ENVISAT SAR data relative to the 2000 and 2006 uplift episodes (D'Auria et al., 2012; Lanari et al., 2004) (Figure 3). The maps represent the line-of-sight deformation along both ascending and descending satellite orbits. Since the aim of this task was to determine the optimal source shape, we compared simulations and data by normalizing them to their RMS. The misfit function was then defined as

$$E(\boldsymbol{m}) = \sum_i \left(d_i^{2000} - sy_i\right)^2 + \sum_j \left(d_j^{2006} - sy_j\right)^2 \tag{12}$$

where d_i^{2000} and d_j^{2006} are the normalized SAR data at the maximum deformation for the 2000 and 2006 uplift episodes, respectively, while sy are the normalized synthetic ground deformation computed for the source geometry $\boldsymbol{m}$.

The best fit model consists of a NE-SW horizontal elongated structure, placed at approximately 2,400-m depth and extending from less than 1 km southwest of Solfatara toward Pozzuoli Bay (see Figure 4b). The source depth has been fixed and has the same value as that used to model the background field (Figure 2). The minimum misfit is reached with an averaged error of 18%.

We must emphasize that the center of the maximum uplift (Trasatti & Bonafede, 2008) is displaced (see the contours in Figure 4b) with respect to the Solfatara crater (star in Figure 4b), which is currently the area with the highest fluid discharge rate (Caliro et al., 2007; Chiodini et al., 2001). This offset suggests that the source of transient ground uplift episodes is different from that driving the background state of the CFc.

In Figure 4b, we show the distribution of the source cells, defined on the basis of the discretization of the thermo-fluid dynamics simulation with TOUGH2.

3.3. Temporal Green's Functions

As noted above, our physical assumption is that transient injection episodes perturb the convective pattern of the system weakly enough to leave the background steady state substantially unchanged. The linearization of the fluid flow equations allows the use of a linear theory to analyze the observed data.

We computed the vertical ground deformation at the center of the caldera and compared it with optical leveling and GPS measurements, which allows extending the data set since 1987 (De Martino et al., 2014; Del Gaudio et al., 2010). Hence, by this process, equations (10) and (11) simplify to

$$\psi(t) = z_{\max}(t) = \int_{-\infty}^{\infty} G_z(\tau; t)\, s(\tau) d\tau \tag{13}$$

where G_z is the Green's function corresponding to the vertical ground deformation at the center of the caldera and s is the source flow rate. Equation (13) represents a simple convolutional problem that has been solved using the technique illustrated in section 4.

The G_z values have been estimated numerically by injecting a batch of a pressurized hot CO_2-rich mixture (H_2O/CO_2 mass ratio of 0.66) from the elongated structure (Voronoi cells in Figures 2, 3, and 4b). The injection rate is 4,000 kg/s, and its duration is 15 days, giving a total amount of 5.2 Gkg. In Figure 4a, we show the numerical Green's function for pure CO_2 and H_2O fluids and for the CO_2-H_2O mixture. All three curves are almost equal; that is, on short temporal scales, injections of different percentages of the two fluids (preserving the total mass) give similar results. From the separate estimation of the effects of thermoelastic and

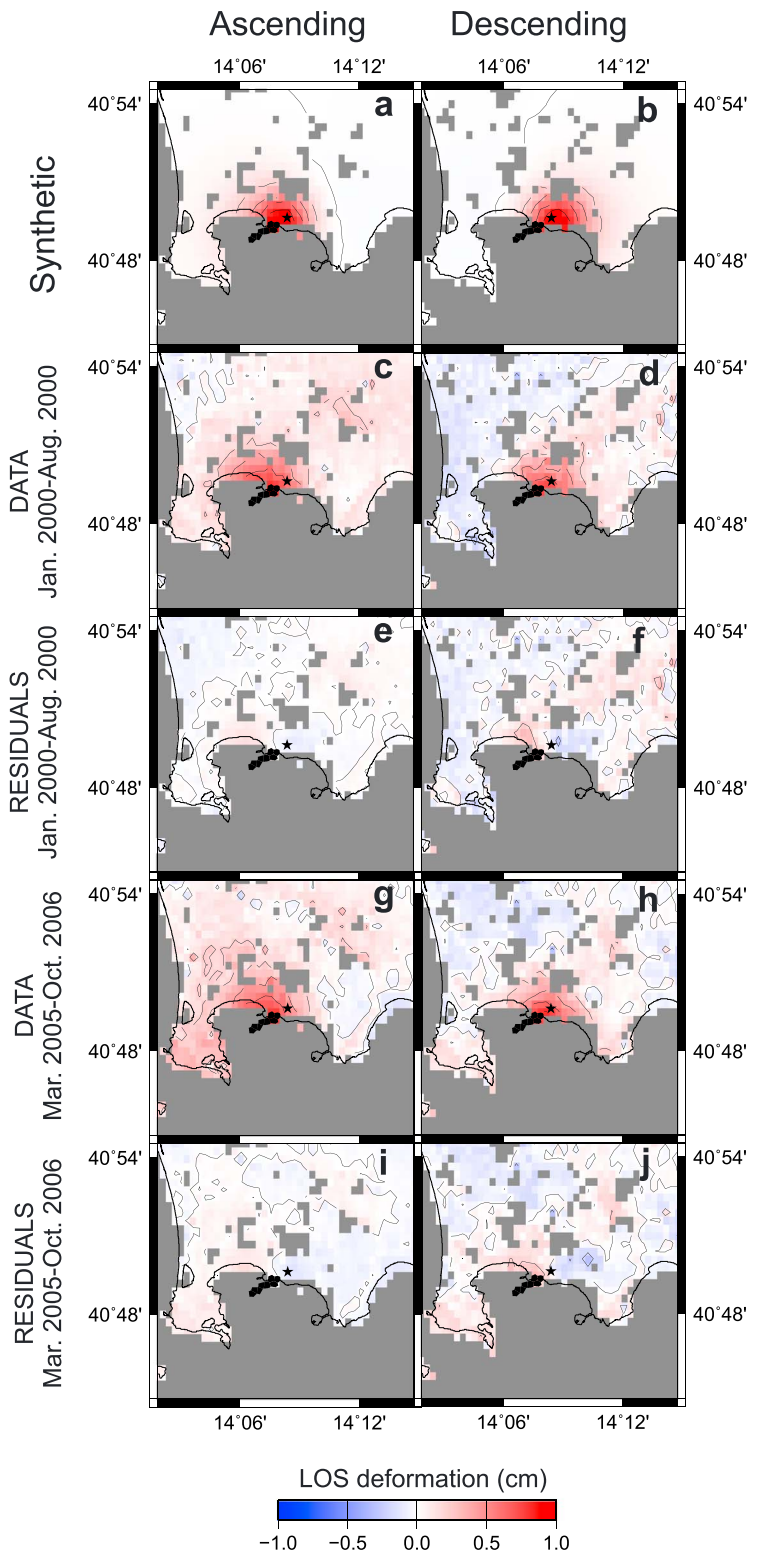

Figure 3. Comparison of the synthetic ground deformation pattern with DInSAR observations related to two deformation episodes (see D'Auria et al., 2012, for a description of the data set). Columns show the ascending orbits and descending orbits of the satellites. Simulated and measured data maps show the normalized components of the line-of-sight (LOS) values (rows 1, 2, and 4). The second and fourth rows are related to the 2000 and 2006 uplift episodes, respectively. Maps in rows 3 and 5 are the residuals between the measured and simulated data; note that we used the same source for both the episodes. The stars indicate the position of Solfatara. The aligned black dots indicate the source shape.

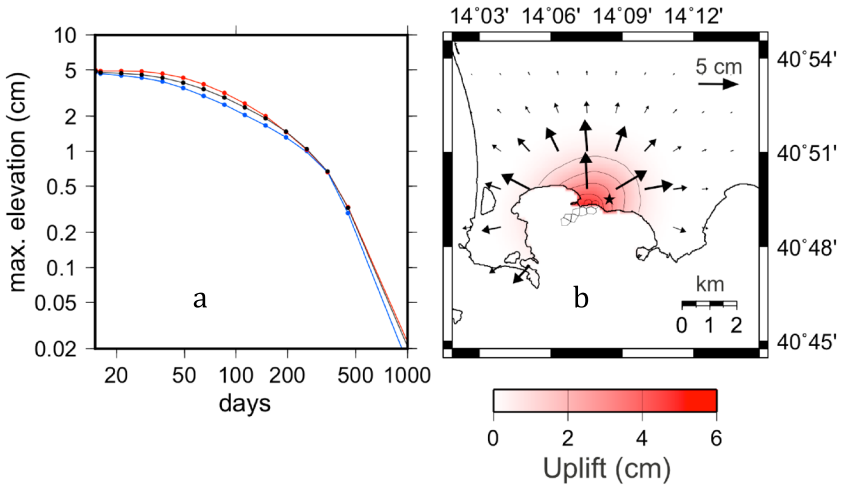

Figure 4. (a) Temporal variation in the maximum ground uplift during the injection of fluids at a rate of 4,000 kg/s for 15 days. The three curves refer to pure H_2O (blue), pure CO_2 (red), and a mixture of both with a H_2O/CO_2 mass ratio of 0.69 (black curve). (b) The map shows the ground deformation pattern at the end of the injection. The shades of color represent the vertical deformation; the arrows represent the horizontal component. The black star indicates the position of the Solfatara crater, while the Voronoi tessellation is the trace of the injection fracture (see section 3 for details).

poroelastic strains, we observe that the poroelastic is largely dominant at the time scales investigated in this work (a few years; Figure 5).

In Figure 6, we represent the temporal evolution of the pressure field and of the streamlines after a 15-day injection of a fluid batch. We observe that the pressure field reaches a peak at the end of the injection. The pressurized volume has an elongated shape reflecting that of the source. The background streamline pattern (at $t = 0$) is slightly distorted in the volume above the source during the injection. Nevertheless, after approximately 130 days, the original steady state stream pattern has been almost fully recovered (Figure 6). It is noteworthy that the main density flux (green cones) remains localized along the vertical axis passing through the Solfatara crater; this result agrees with measurements in the CF caldera confirming that the system quickly comes back to the original state.

To prove the validity of our linear approach as regard the magnitude of the injected fluids, we injected different amounts of the CO_2-rich mixture (H_2O/CO_2 mass ratio of 0.66). The duration of injections is 15 days for all the four injections, and the flow rates are 5,360, 1,720, 320, and 120 kg/s. Each fluid injection starts from the same thermo-fluid dynamical condition (steady state). We calculated the z pattern as a function of time, of the maximum deformation point on the surface for the four above cases. As seen in Figure 7a, the behavior of the four curves with time has similar trends considering both the ascent branches and descent ones. This behavior is satisfied along the entire deformation pattern, not only for the maximum uplift point (see Figures A3, A4, A5, A6, and A7).

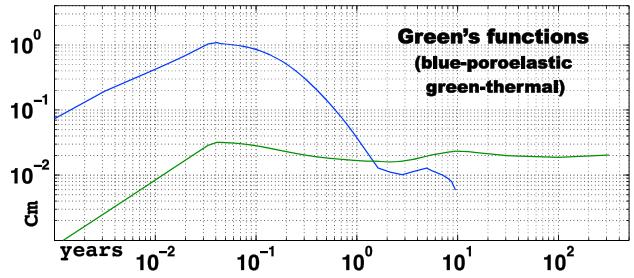

Figure 5. Temporal variations in the maximum ground uplift during the injection of fluids (H_2O/CO_2 mixture) at a rate of approximately 800 kg/s for 15 days. The blue curve is the deformation due to the poroelastic effect only, while the green curve is the deformation due to the thermoelastic effect only.

In particular, to verify the validity of the linearization, we use the curve relative to the deformation with the smallest source (120 kg/s), comparing it with the deformation curves for the other three cases. We represent in Figure 7b the plots of the deformations for the three other cases versus the first one. The linearity evidently holds since the points align along straight lines with the angular coefficients equal to the ratio of the injected amount to the amount of the reference source (the smallest with 120 kg/s).

We have also explored (see Appendix A) the sensitivity of the Green's function, varying the permeability and porosity parameters in a 3-D uniform domain. We have found that porosity variations in the 10–40% range produce errors within a factor of 2, while permeability variations in the 10^{-12}–10^{-16} m^2 range can give estimates of the injected fluids that vary

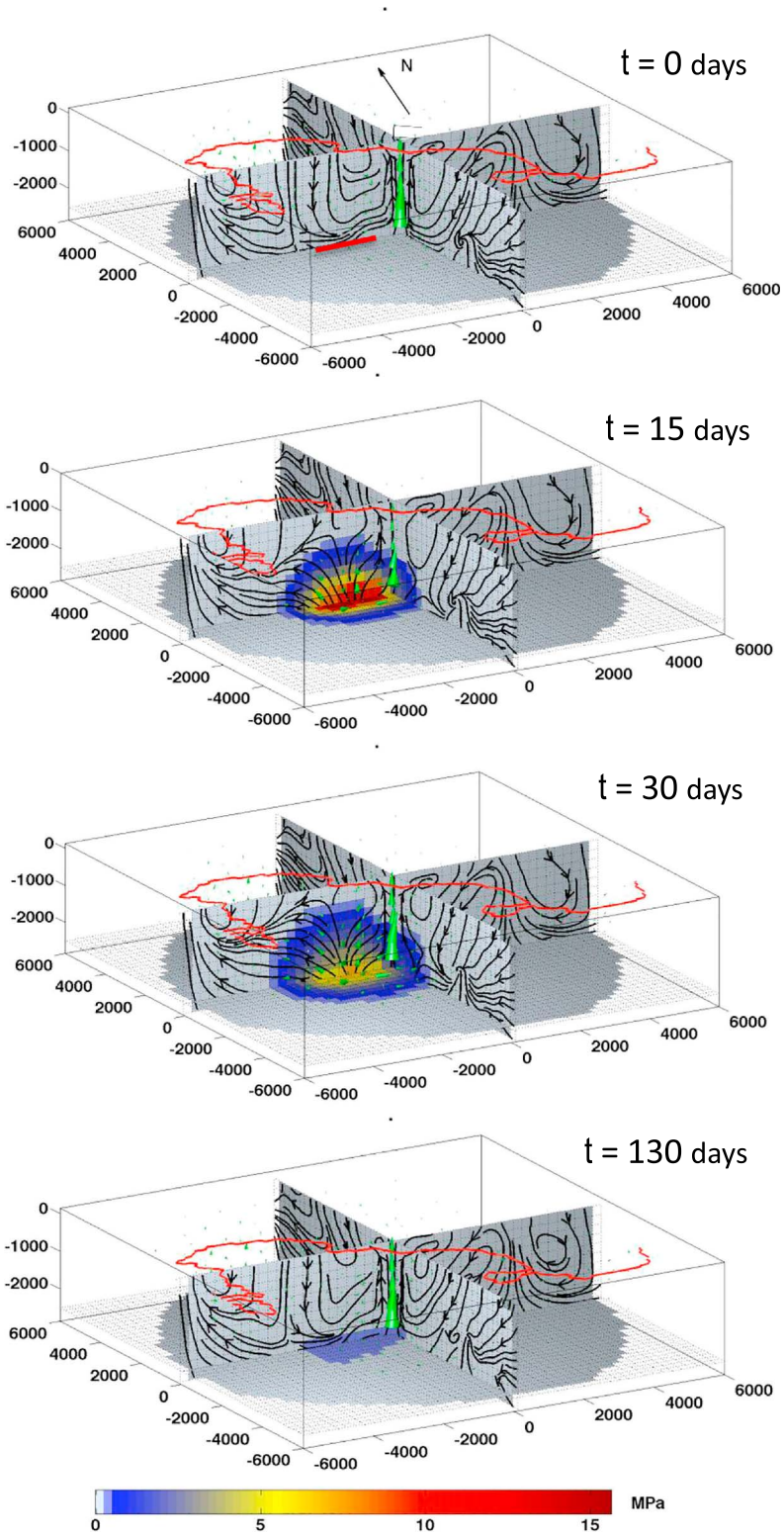

Figure 6. 3-D representations of the pressure variations and the flow patterns after a fluid injection episode, where *t* is the time in days. The black arrow indicates north; the black star shows the position of Solfatara (0,0,0 coordinate for the computational model), the red line marks the coast of CF caldera, and the thick red straight line represents the position of the injection fracture. The green cones show the fluid flow patterns, and dimensions are proportional to the flow magnitude. The flow corresponding to the larger cone is approximately 0.32×10^{-2} kg/(s m^2). The two cross sections represent both the pressure variations (color scale at the bottom) and the flow patterns (streamlines).

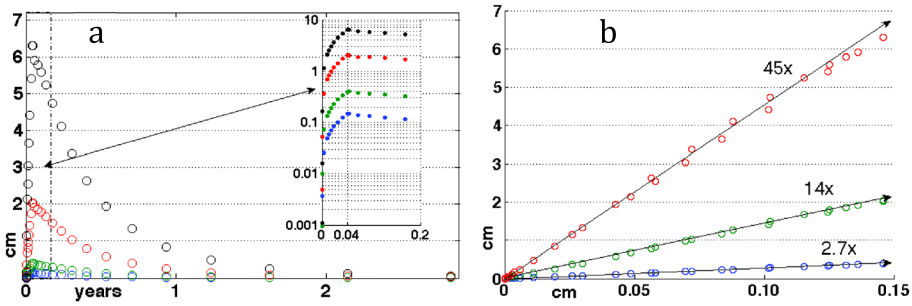

Figure 7. (a) Temporal pattern of the maximum deformation point on surface related to the 3-D elastic model of the Campi Flegrei caldera. The curves were obtained by injecting into the source cells (q_1) four different amounts of fluids (black circles 5,360, red circles 1,720, green circles 320, and blue circles 120, in kg/s, with a H_2O/CO_2 mass ratio of 0.69). (b) Plot of the ground deformations associated with the three larger injections vs. the deformation due to the smaller injection.

by an order of magnitude. Knowledge of the correct permeable-porous model is hence crucial for the applicability of the method to real cases. Our test case is CFc, where most of the observed deformation events, with time scales of 10^0–10^1 years, have been ascribed to hydrothermal system perturbations that follow the injection of hot, magmatic fluids (mainly CO_2-H_2O mixtures) at depth (Chiodini, 2009; Chiodini et al., 2003, 2012). In particular, in the following section, we will demonstrate the stability of the elastic response of the system to repeated injections. This condition is essential to define the linearity with respect to time.

4. Inverse Method and Synthetic Test

In this section we discuss and demonstrate the invariance, with respect to time, of the Green's function. In addition, we confirm the linear response of the system to different pulses, also when they are multiple and repeated over time.

We now show how to exploit the observed temporal variations in the ground deformation (z_{max}) to retrieve the fluid injection rates (s).

In the following, we use a synthetic test to demonstrate that, in our case, the linearized approach has a range of validity of approximately 15–20 years. Over longer time scales, repeated perturbations of the hydrothermal system could cause permanent modifications in the thermodynamic variables, invalidating the linearized approach.

We discretize the convolutional model for the observed ground deformation as follows:

$$z_{max}(t_k) = \sum_{i=0}^{N} s(t_{k-i})\Gamma(t_i) \tag{14}$$

where $\Gamma(t)$ is the numerical Green's function and N is the number of time samples. We have discretized a period of 26 years, of the same duration as the CF time series, into 631 samples with a sampling interval of 15 days. For numerical purposes, Green's function has been discretized using the same sampling. The previous equation can be written in matrix form as $z = \Gamma s$, where Γ is an $N \times N$ matrix, z represents the discretized data, and s is the unknown source function.

We solve this problem using a truncated single value decomposition approach (Aster et al., 2004). This technique allows regularizing the estimated model of the inverse problem by removing the singular eigenvalues from the generalized inverse matrix. Selection of the correct number of eigenvalues, used for the inversion, was found using the L-curve method. The number of selected eigenvalues has been chosen using the Akaike information criterion (Akaike, 1974). In our case, the Akaike information criterion indicates approximately 100 eigenvalues as the best estimate.

We note that the solution vector s needs to respect a nonnegativity constraint: negative flow values are meaningless from a physical point of view. We have implemented this constraint by exploiting the approach of Lawson and Hanson (1974).

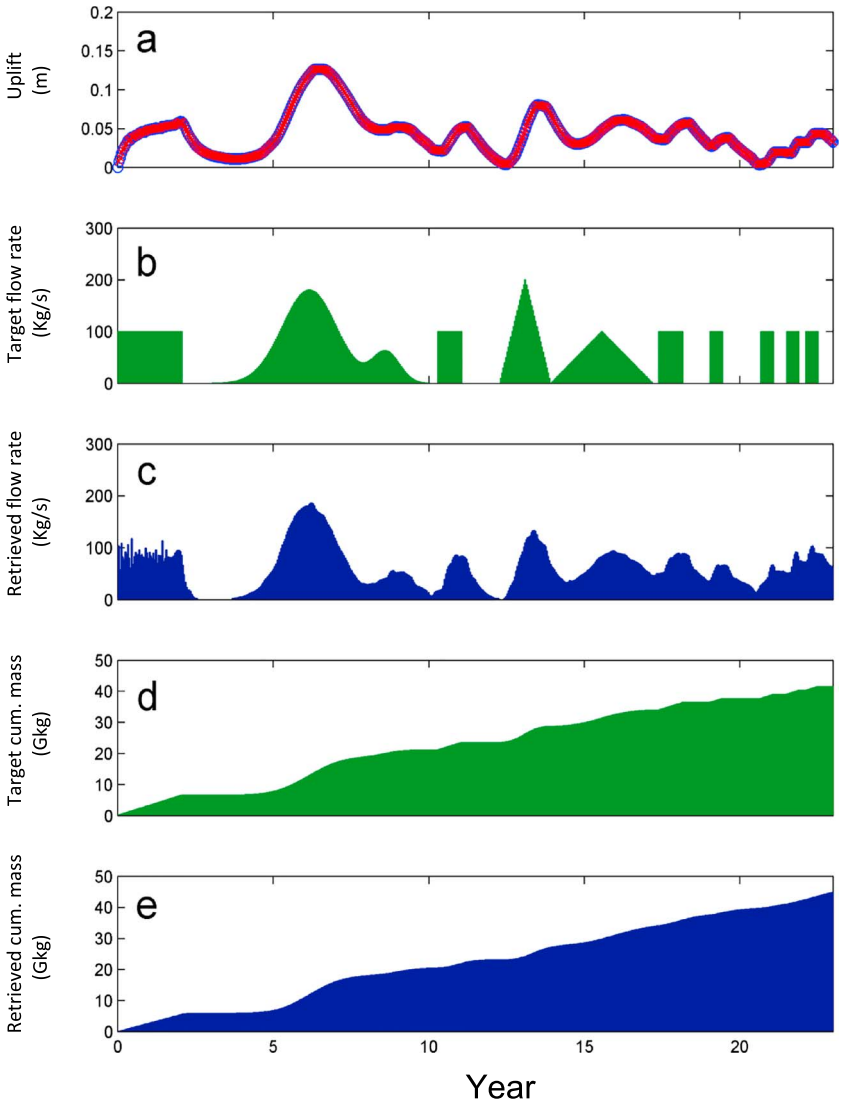

Figure 8. Results of the synthetic test. (a) Target ground deformation (blue) and the retrieved values (red). (b) Flow rate pattern used to compute the target ground deformation in a. (c) Retrieved flow rate obtained inverting the target ground deformation. (d) Target cumulative injected masses. (e) Retrieved cumulative injected masses.

We have tested this approach with a simulated data set. Using the synthetic flow rate pattern shown in Figure 8b, we have performed the forward modeling described above. That is, using TOUGH2 code we injected into the model (Figure 2), throughout the source elements, the flow rate represented in Figure 8b. Then we compute by COMSOL the synthetic ground deformation time series shown in Figure 8a; each point represents the maximum value of the deformation on the surface versus years. Note that this pattern, as function of time, is invariant with respect to the x,y coordinate except for a scale factor (Appendix Figures A3, A4, A5, A6, A7). This series has been inverted ($s = \Gamma^{-1}z$), that is throughout the inversion of the equation (14), we obtain the estimated source flow rate of Figure 8c. Even if repeated injections alternating with short periods of quiet are poorly separated, the main characteristics of the synthetic source (Figure 8b) are correctly estimated. The agreement holds also between the estimated and the synthetic cumulative curves (Figures 8d and 8e). Figure A9 shows the estimate of the associated error.

5. Application to the Whole 1987–2013 Ground Deformation Data Set

Finally, we have extended the application of the method to the whole 1987–2013 data set. We assume that this deformation time series consists of two different components having distinctive time scales: the first

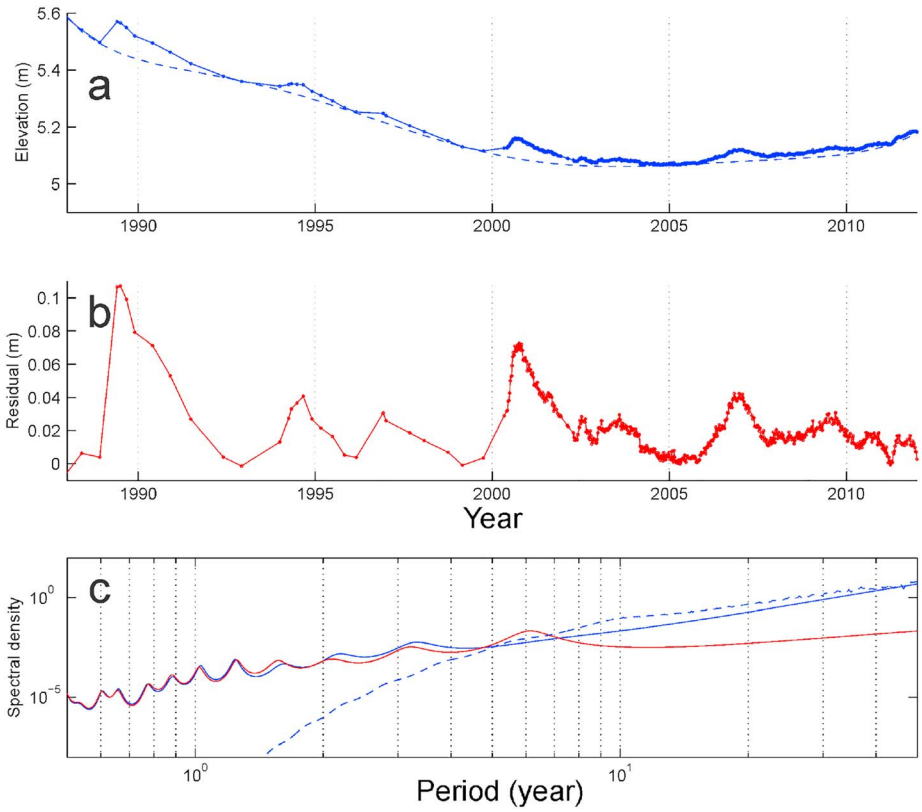

Figure 9. Ground deformation data set. (a) The blue curve shows the observed ground deformation at the point of maximum uplift. The blue points represent individual measurements. The dashed blue line is the polynomial fit (see section 5 for details). (b) Residual ground deformation after the removal of the polynomial fit. (c) Maximum-entropy spectra for the original data (blue curve), the polynomial fit (dashed blue line), and the residuals (red curve).

one takes into account the long-term trend, and the second one includes the short-term (<5 years) bumps in the time series (Figure 9). While the long-term component could be attributed to the release of magmatic fluids following the marked 1982–1984 inflation ascribed to the exolution of hypersaline brine and gas located as a lens at approximately 3-km depth (Battaglia et al., 2006), the short-term component has been related to the injection of new hydrothermal fluids (Chiodini et al., 2012; D'Auria et al., 2012, 2015).

To separate the two components, we used a fifth-order polynomial constrained to match the relative minima of the time series (Figure 9a). From the spectral analysis of the original data, the polynomial fit, and the residuals (Figure 9c), it can be seen that this filtering procedure allows a good separation between short-term (<5 years) components and the long-period trend.

Todesco et al. (2004, 2010) and Todesco (2009), who previously combined TOUGH2 and deformation modeling, showed how repeated fluids injection in the Campi Flegrei hydrothermal system could explain the short-term deformation path. In our inverse scheme we give a method that quantitatively estimates the injected fluids into the hydrothermal system from the observed deformation pattern.

Figure 10a shows that the true deformation pattern matches well with the synthetic data estimated by the inversion procedure. The retrieved flow rate (Figure 10c) has been used as input for a thermo-fluid dynamics simulation.

From the results of this time-varying simulation, we have computed the synthetic ground deformation time series (Figure 10b) using the procedure described in section 3. The simulated deformation pattern (Figure 10b) shows good agreement with the measured time series (Figure 10a), demonstrating that our linearized approach provides a good approximation for the thermo-fluid dynamics modeling of hydrothermal systems; the associated error gives a misfit of approximately 20%. The main differences are found toward the end of the simulated period and consist of a persistent deformation of approximately 2 cm. This result can be

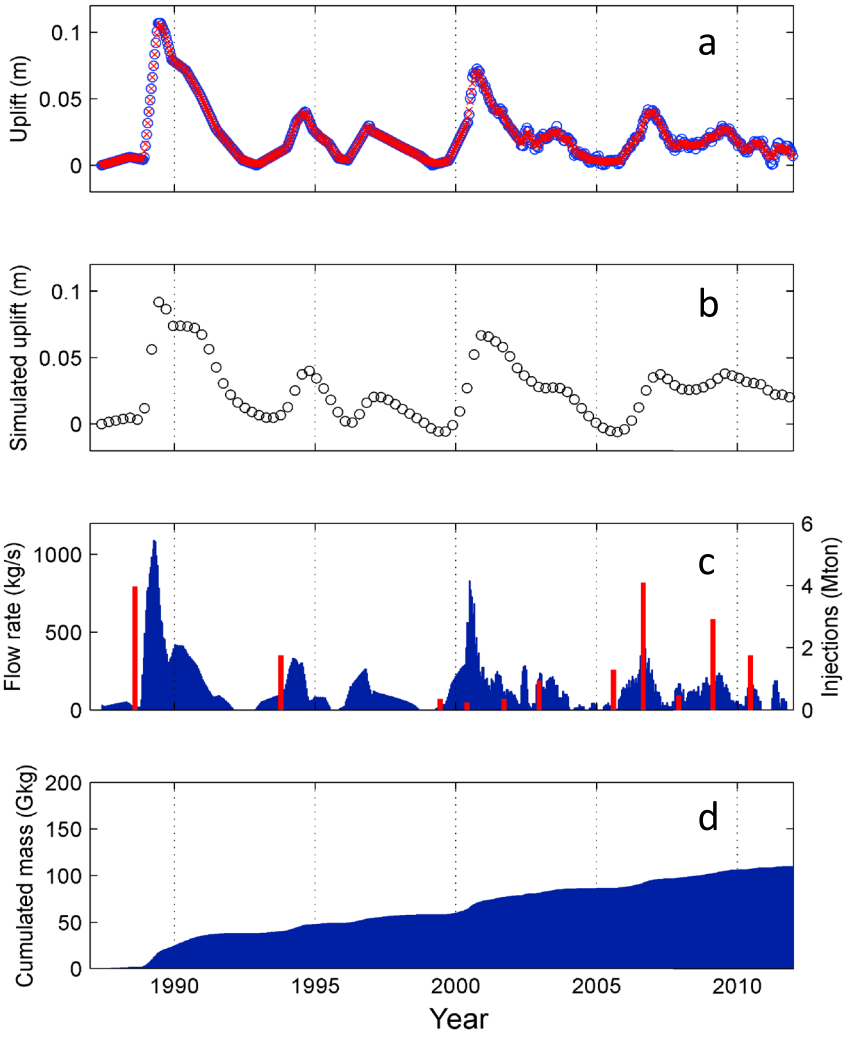

Figure 10. Results of the inversion on the Campi Flegrei caldera data set. (a) True data (blue circles) and inversion results (red Xs). (b) Simulated ground deformation pattern using the estimated flow rates. (c) Estimated flow rate pattern. The red bars on this plot are the injections retrieved by Chiodini et al. (2012) using a trial-and-error approach to fit observed geochemical time series. The scale for the injections is on the right. (d) Cumulative mass of the retrieved injection rate.

explained by invoking a progressive deviation from the background steady state because of the repeated injections. Indeed, as we have already stated in section 2, the basic assumptions of the perturbative formulation begin to lose validity over long time intervals (approximately 15 years).

Figure 10c compares the estimated flow rates with the previously retrieved injections, using a trial-and-error approach to fit the observed geochemical time series (i.e., fumarolic compositions; for further explanations, see Chiodini et al., 2012). The figure highlights good matches between the two independent series for the first events in 1990 and 1994 and for the sequence of injections that occurred after 2005 (note that the Chiodini et al., 2012, simulation ended in 2010, i.e., before the last deformation peak). The deformation peak that occurred in 1996–1997 does not correspond to any geochemically derived event, but in this period, the discrepancy can be due to a break in the compositional series of Solfatara fumaroles. The only evident difference is seen in the deformation events of 2000, when the high fluxes estimated with the new approach correspond to geochemically retrieved events of much lower magnitude. This outcome is not surprising because it has already been noted (D'Auria et al., 2011) that the 2000 uplift episode did not cause strong geochemical anomalies, most likely because it was caused by a pressurization event not followed by a corresponding fluid injection in the fumarolic system of Solfatara. This observation points to an obvious limit for the new approach: it cannot work correctly if the inflation pulse is caused by a deep process of

pressurization not followed by fluid transfer in the upper portion of the system. In any case, it has to be underlined that the method involves the entire amount CO_2/H_2O injected into the geothermal system of the CF caldera, while in geochemical works similar to Chiodini et al. (2012), the estimates are made in a more restricted area (a few km^2). Presumably, these considerations should be a stimulus for geochemical campaigns extended to areas comparable with the extent of the whole caldera.

6. Conclusions

Fluid injections are the possible source mechanism for deformation in active calderas (Bonafede, 1991; D'Auria et al., 2012; Hurwitz et al., 2007). This work successfully focused on the development of a tool able to quantitatively estimate the fluid injection rate from the observed ground deformation.

In section 2, we briefly outlined the mathematical background of the perturbative approach to nonlinear fluid dynamics problems, discussing the general validity conditions. We explored (Appendix A) the sensitivity of Green's function, varying the permeability and porosity parameters in a 3-D uniform domain. We found that porosity variations in the 10–40% range produce errors within a factor of 2, while permeability variations in the 10^{-12}–10^{-16} m^2 range can give estimates of the injected fluids that vary by an order of magnitude. Knowledge of the correct permeable-porous model is hence crucial for the applicability of the method to real cases. Our test case is CFc, where most of the observed deformation events, with time scales of 10^0–10^1 years, have been ascribed to hydrothermal system perturbations that follow the injection of hot, magmatic fluids (mainly CO_2-H_2O mixtures) at depth (Chiodini, 2009; Chiodini et al., 2003, 2012). The areas of the most intense degassing at Campi Flegrei do not coincide with the area of maximum ground deformation. Exploring the whole model space constraining the single source, the alignment of the source cells, and a common source flow rate for each cell, we have matched the observed SAR deformation pattern with the synthetic model, determining the source shape and position. Our finding is that the fluids responsible for the short-term (<5 years) deformation patterns are released at a depth of approximately 2,400 m from an elongated fracture located approximately at the center of the caldera (Figure 3). This result suggests that the fluids injected along the fracture are essentially transported by a preexisting convective flow pattern dominated by the ascending plume below the Solfatara crater (Figure 6). Using a steady state model of the CFc hydrothermal system (Petrillo et al., 2013) as a reference background, we estimate the injection rates of the hot volcanic fluids for the last 25 years (Figure 10) at the CFc.

The linear inverse procedure used, based on numerical Green's functions, correctly models the measured deformation time series. The comparison between the modeled injection events and the events previously simulated with a purely geochemical approach (Chiodini et al., 2012) highlights a good correspondence between the two independent results, with the only significant difference regarding the event in 2000, which was probably produced by a relatively deep pressurization process without significant fluid transfer in the overlying hydrothermal system. In spite of this discrepancy, the new results confirm one of the main findings reported in Chiodini et al. (2012): the amount of fluids involved in each degassing event is of the same order of magnitude (10^0–10^1 Gkg) as that involved in the low- to medium-size eruptions.

In conclusion, the linearized approach used in this work shows promising prospects for the study of short-term perturbations of hydrothermal systems, and in particular, it can be useful for volcano and geothermal monitoring applications, allowing a quick quantification of mass and energy budgets during episodes of volcanic unrest and hence providing a valuable tool for decision makers.

Appendix A

In this section, we show the dependency of Green's function on two parameters: permeability and porosity. The simulations are based on a 3-D domain (see Figure 2) with a uniform distribution of the two parameters, varying the permeability of the model from 10^{-12} to 10^{-16} m^2 and the porosity from 10 to 40%.

The thermodynamic initial conditions are 0.09 °C/m for the temperature gradient and 9,000 Pa/m for the pressure gradient. We have injected water with an enthalpy of 2.6×10^6 Joule/kg at a depth of 2,550 m neglecting the amount of CO_2, as we have found that Green's function depends (at least for a limited time

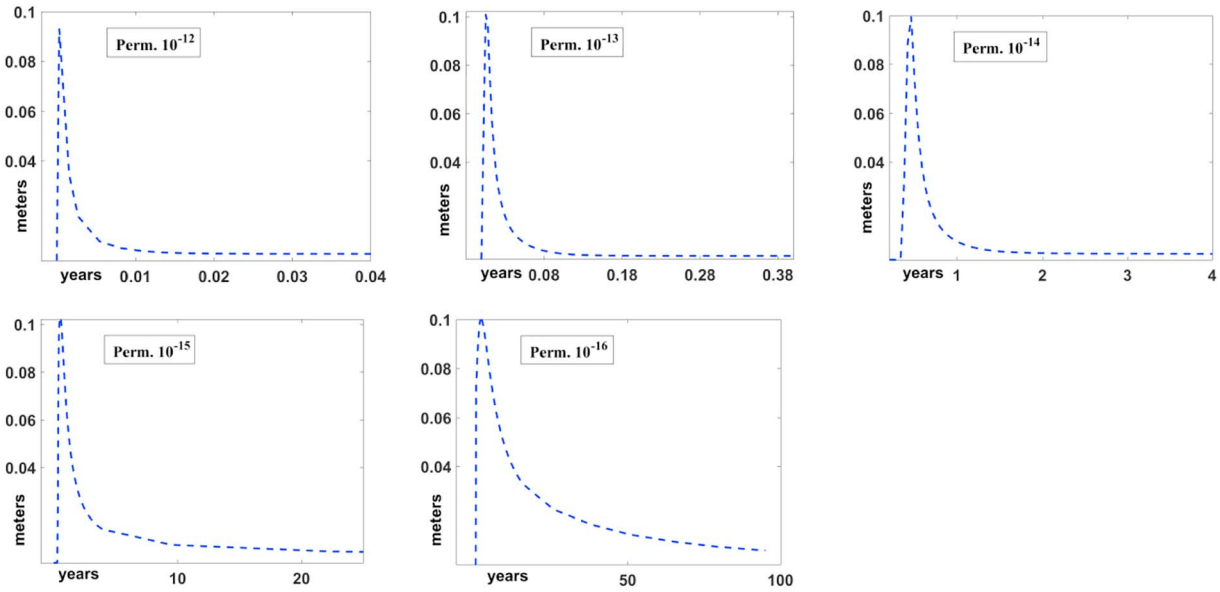

Figure A1. Numerical simulations showing the dependence of Green's function on permeability. The figures show the maximum vertical deformation at the surface as function of time after the injection of a batch of fluid. The strong difference among all the deformation responses is evident. Low permeability largely expands the deformation response.

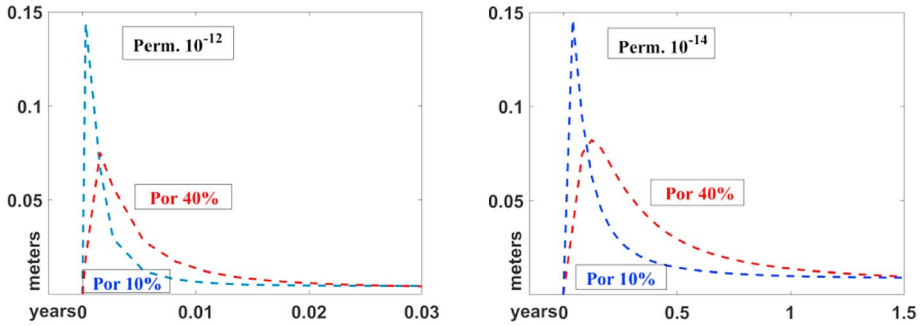

Figure A2. Numerical simulations showing the dependence of Green's function on permeability and porosity. The figures show the maximum vertical deformation at the surface as function of time after the injection of a batch of fluid. Green's function expands and shortens in both simulations as porosity increases.

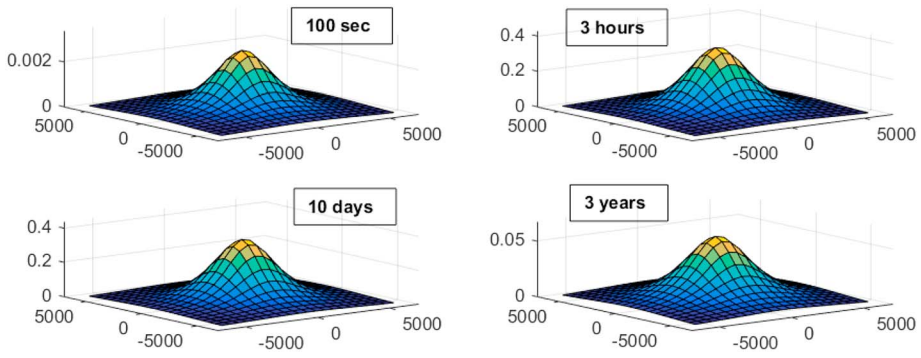

Figure A3. Numerical simulations showing the *z*-deformation pattern due to an injection at 2,550-m depth. The vertical scales are different to show the high similarity among the patterns.

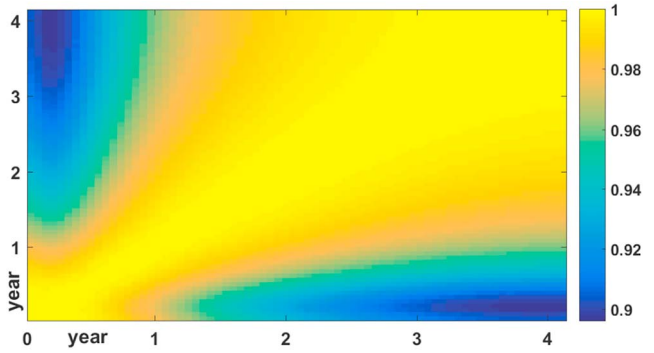

Figure A4. Correlation coefficients matrix obtained among the snapshots of z-deformation patterns due to an injection at 2,550-m depth in the temporal interval [0 4] years. The model has a porosity of 10% and a permeability of 10^{-14} m^2.

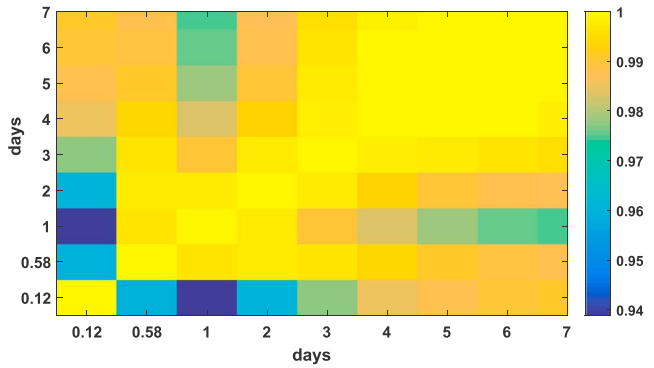

Figure A5. Correlation coefficients matrix obtained among the snapshots of z-deformation patterns due to an injection at 2,550-m depth in the temporal interval [0, 8] days. The model has a porosity of 10% and a permeability of 10^{-12} m^2.

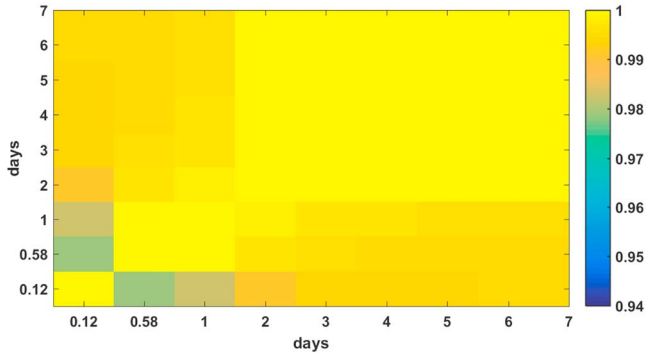

Figure A6. Correlation coefficients matrix obtained among the snapshots of z-deformation patterns due to an injection at 2,550-m depth in the temporal interval [0 8] days. The correlation analysis is limited to pixels included in an 8-km diameter around the injection source. The model has a porosity of 10% and a permeability of 10^{-12} m^2.

interval) almost completely on the amount of the injected mass, rather than on the proportions of the two components (Figure 4a).

In Figure A1, we show the results of a set of simulations based on five different models with a homogeneous distribution of permeability. The deformation calculated for a point at the surface (corresponding to the injection point at depth) of an elastic uniform half-space with a shear modulus of 8×10^9 Pa is shown. The durations of the two deltas (pulses of injections) are approximately 30 days for the three simulations related to the low-permeability models, while for the model with the higher permeability (10^{-12} m^2), the duration is several hours. Moreover, we have constrained the amount of the injected fluid, fixing the value at approximately 10^{10} kg for all five simulations. In the inverse procedure, the duration of the delta function must be much less than the relaxation time to allow a correct reconstruction of the injected fluid history. The strong difference among all the deformation responses is evident, with trends depending on the permeability value assigned to the model. As expected, low permeability greatly widens the deformation response. Low permeability also confines fluids in the injection zone, increasing the duration of the pressure pulse. Conversely, high permeability allows a rapid decrease in the pressure near the source. This dependency implies the need for knowledge about permeability for the application of our method to real cases to obtain a correct estimate for the amount of injected fluids.

In Figure A2, we show the results of tests on two models with permeabilities of 10^{-12} and 10^{-14} m^2 and porosities of 10% and 40%. The behavior of the delta function has a common characteristic: as the porosity increases, the delta widens depending on the assigned porosity values, and the amplitude decreases with increasing porosity. Although the response depends even on the porosity, this variable has values that do not affect the order of magnitude of Green's function. The permeability remains the more critical parameter.

The basic assumption of our method is that the uplift of each surface element is correlated to all the others; on this basis, we can analyze the temporal pattern of each single element as representative of all the surface, in particular. To test our hypothesis about the stability of the deformation temporal pattern, we have simulated an injection episode of approximately 10^{10} kg at 2,550-m depth in a half-space with a permeability of 10^{-14} m^2, a porosity of 10%, and a shear modulus of 3×10^9 Pa. In Figure A3 four snapshots of the deformation due to an injection of hot water at a constant rate of 10^6 kg/s for approximately 10^4 s are shown.

After approximately 3 hr (the end of the injection), the deformation remains at the same level for up to 10 days and then slowly decreases, but the shape remains almost the same. To evaluate the degree of correlation, we show the correlation matrix (Figure A4) among all the snapshots (100) spanning the times from $t = 0$ to approximately $t = 4$ years. A correlation of 1 implies that all the deformation patterns are linearly dependent on each other. Our results show that there is a very good general correlation among the snapshots; the worst results with a minimum correlation equal to 0.9 happen when we compare the first snapshots with the last snapshots relative to time on the order of years.

In Figure A5, we show the values of the correlation matrix relative to a case where the homogeneous half-space has a porosity of 10% and a permeability of 10^{-12} m^2; the process of inflation and deflation is very

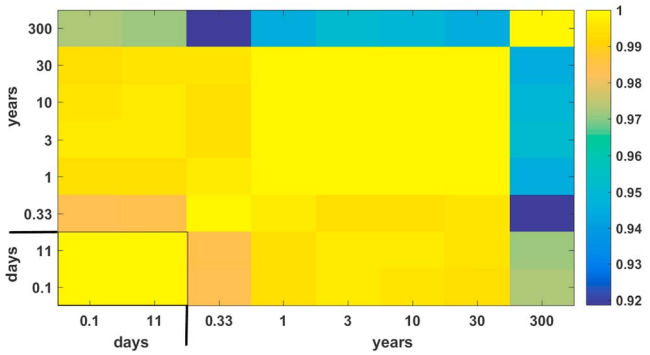

Figure A7. Correlation coefficients matrix obtained among 8 snapshots of z-deformation patterns due to an injection (5×10^9 kg in 10^6 s) at 2,550-m depth in the temporal interval [0 300] years. The model has a porosity of 10% and a permeability of 10^{-15} m^2.

quick (see the case for 10^{-12} m^2 in Figure A1). In this case, the very good correlation is evident as the lower correlation is 0.94.

In any case, the decrease in correlation depends on the pixel of the snapshots farther from the point source. If we reduce the analysis to a diameter of 8 km around the source, the mean value of the correlation matrix strongly increases with a minimum of correlation equal to 0.98 (Figure A6).

In the last figure (Figure A7), we show the correlation matrix in a case with the permeability value set to 10^{-15} m^2; this case is closer to our mean value of permeability used for the real case. To better follow the nature of the phenomenon, we use snapshots with increasing temporal interval.

Our results show that for up to 30 years, the correlation among the snapshots is greater than 0.98, while the z-deformation reduces the correlation value to 0.92 only when we consider the deformation hundreds of years after the injection.

In the following figure (Figure A8) we show an enhanced color map of the residuals relative to the e, f, i, and j subplots of Figure 3 in the text.

At this order of approximation we can appreciate the difference between the modeled and measured deformation pattern. This remaining deformation field, not explained by the source we have found, seems to have a multipolar behavior. In any case it seems that the shape of this residual field appears again stable in the two episodes even with some differences.

Finally, we show (in Figure A9) the relative and absolute error on the injected flux of hot fluid into the hydrothermal system. The error is estimated by the comparison of the reconstructed amount (inversion scheme) of injected mass (Figure 8e) with the injected fluid in the simulator TOUGH2 (Figure 8d).

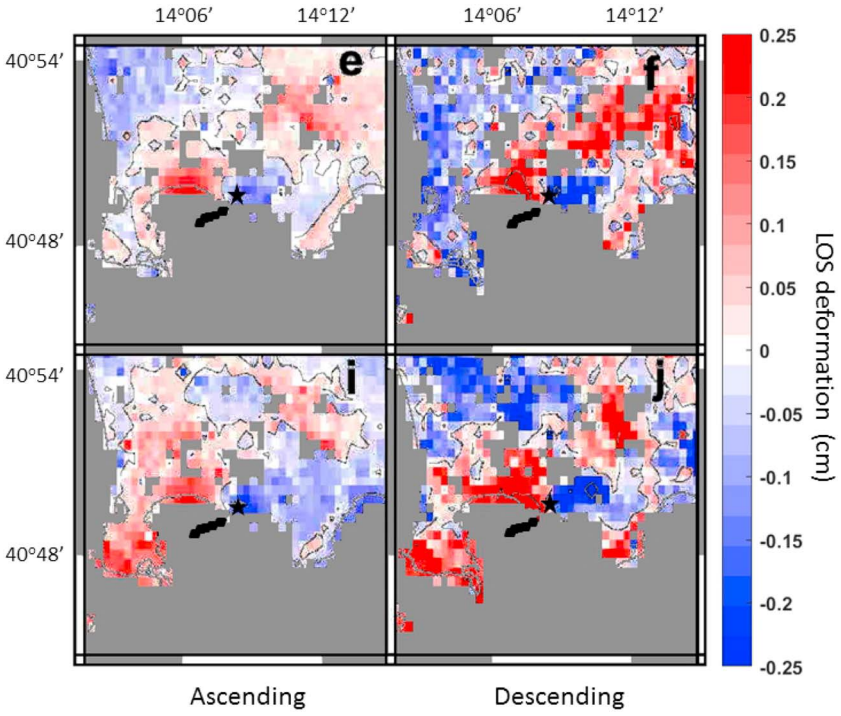

Figure A8. Residuals maps representing the e, f, i, and j subplots of Figure 3 in the text, with different residuals scale. The stars indicate the position of the Solfatara crater. The aligned black dots indicate the source shape.

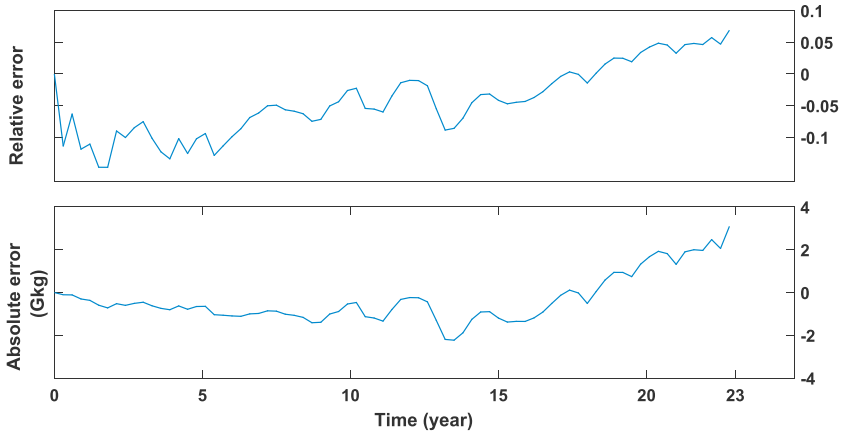

Figure A9. Estimation of the error on the amount of injected fluids, when using the linear approach and the inversion scheme. The relative averaged error is 3.7%, and the absolute maximum error, about 3 Gkg, is reached at the end of the simulation.

Acknowledgments
This work was financially supported by the MED-SUV project. SAR data were provided by CNR, Italy. We truly thank the Editor, Michael Walter, Lauriane Chardot (reviewer), an anonymous reviewer, and Maurizio Battaglia (previous reviewer) for their constructive criticism and the detailed revision, which greatly improved our manuscript. Data used for this study (Vp, Vs, density, porosity, and permeability tomography of the CFc) are available in the attached supporting information.

References

AGIP. (1987). Modello geotermico del sistema flegreo. Servizi Centrali per l'Esplorazione, SERG-MESG, San Donato, 23 pp. (in Italian). Agip Oil Company.

Akaike, H. (1974). A new look at the statistical model identification. *IEEE Transactions on Automatic Control*, *19*(6), 716–723. https://doi.org/10.1109/TAC.1974.1100705

Amoruso, A., Crescentini, L., & Sabbetta, I. (2014). Paired deformation sources of the Campi Flegrei caldera (Italy) required by recent (1980–2010) deformation history. *Journal of Geophysical Research: Solid Earth*, *119*, 858–879. https://doi.org/10.1002/2013JB010392

Amoruso, A., Crescentini, L., Sabbetta, I., De Martino, P., Obrizzo, F., & Tammaro, U. (2014). Clues to the cause of the 2011–2013 Campi Flegrei caldera unrest, Italy, from continuous GPS data. *Geophysical Research Letters*, *41*, 3081–3088. https://doi.org/10.1002/2014GL059539

Aster, R., Borchers, B., & Thurber, C. (2004). *Parameter estimation and inverse problems* (2nd ed., p. 301). Waltham, MA: Academic Press.

Barberi, F., Corrado, G., Innocenti, F., & Luongo, G. (1984). Phlegraean fields 1982–1984: Brief chronicle of a volcano emergency in a densely populated area. *Bulletin of Volcanology*, *47*(2), 175–185. https://doi.org/10.1007/BF01961547

Barberi, F., Innocenti, F., Lirer, L., Munno, R., Pescatore, T., & Santacroce, R. (1978). The Campanian Ignimbrite: A major prehistoric eruption in the Neapolitan area (Italy). *Bulletin of Volcanology*, *43*, 107–120.

Battaglia, M., Troise, C., Obrizzo, F., Pingue, F., & De Natale, G. (2006). Evidence for fluid migration as the source of deformation at Campi Flegrei caldera (Italy). *Geophysical Research Letters*, *33*, L01307. https://doi.org/10.1029/2005GL024904

Bonafede, M. (1991). Hot fluid migration, an efficient source of ground deformation: Application to the 1982–1985 crisis at Campi Flegrei Italy. *Journal of Volcanology and Geothermal Research*, *48*(1-2), 187–198. https://doi.org/10.1016/0377-0273(91)90042-X

Caliro, S., Chiodini, G., Moretti, R., Avino, R., Granieri, D., Russo, M., & Fiebig, J. (2007). The origin of the fumaroles of La Solfatara (Campi Flegrei, South Italy). *Geochimica et Cosmochimica Acta*, *71*(12), 3040–3055. https://doi.org/10.1016/j.gca.2007.04.007

Casertano, L., Oliveri, A., & Quagliariello, M. T. (1977). Hydrodynamics and geodynamics in the Phlegrean Fields area of Italy. *Nature*, *264*, 161–164.

Chiodini, G. (2009). CO_2/CH_4 ratio in fumaroles: A powerful tool to detect magma degassing episodes at quiescent volcanoes. *Geophysical Research Letters*, *36*, L02302. https://doi.org/10.1029/2008GL036347

Chiodini, G., Avino, R., Caliro, S., & Minopoli, C. (2011). Temperature and pressure gas geoindicators at the Solfatara fumaroles (Campi Flegrei). *Annals of Geophysics*, *54*, 2. https://doi.org/10.4401/ag-5002

Chiodini, G., Caliro, S., Cardellini, C., Granieri, D., Avino, R., Baldini, A., et al. (2010). Long term variations of the Campi Flegrei (Italy) volcanic system as revealed by the monitoring of hydrothermal activity. *Journal of Geophysical Research*, *115*(B3), B03205. https://doi.org/10.1029/2008JB006258

Chiodini, G., Caliro, S., De Martino, P., Avino, R., & Gherardi, F. (2012). Early signals of new vol- canic unrest at Campi Flegrei caldera? Insights from geochemical data and physical simulations. *Geology*, *40*(10), 943–946. https://doi.org/10.1130/G33251.1

Chiodini, G., Frondini, F., Cardellini, C., Granieri, D., Marini, L., & Ventura, G. (2001). CO_2 degassing and energy release at Solfatara volcano, Campi Flegrei, Italy. *Journal of Geophysical Research*, *106*, 213–221. https://doi.org/10.1029/2001JB000246

Chiodini, G., Paonita, A., Aiuppa, A., Costa, A., Caliro, S., De Martino, P., et al. (2016). Magmas near the critical degassing pressure drive volcanic unrest towards a critical state. *Nature Communication*, *7*, 13712. https://doi:10.1038/ncomms13712

Chiodini, G., Todesco, M., Caliro, S., Del Gaudio, C., Macedonio, G., & Russo, M. (2003). Magma degassing as a trigger of bradyseismic events: The case of Phlegrean Fields (Italy). *Geophysical Research Letters*, *30*(8), 1434. https://doi.org/10.1029/2002GL016790

Chiodini, G., Vandemeulebrouck, J., Caliro, S., D'Auria, L., De Martino, P., Mangiacapra, A., & Petrillo, Z. (2015). Evidence of thermal-driven processes triggering the 2005–2014 unrest at Campi Flegrei caldera. *EPSL*, *414*, 58–67. https://doi.org/10.1016/j.epsl.2015.01.012

Corrado, G., Guerra, I., Lo Bascio, A., Luongo, G., & Rampoldi, F. (1977). Inflation and microearthquake activity of Phlegrean Fields, Italy. *Bulletin of Volcanology*, *40*(3), 169–188. https://doi.org/10.1007/BF02596998

D'Auria, L., Giudicepietro, F., Aquino, I., Borriello, G., Del Gaudio, C., Lo Bascio, D., et al. (2011). Repeated fluid-transfer episodes as a mechanism for the recent dynamics of Campi Flegrei caldera (1989–2010). *Journal of Geophysical Research*, *116*, B04313. https://doi.org/10.1029/2010JB007837

D'Auria, L., Giudicepietro, F., Martini, M., & Lanari, R. (2012). The 4D imaging of the source of ground deformation at Campi Flegrei caldera (southern Italy). *Journal of Geophysical Research*, *117*, B08209. https://doi.org/10.1029/2012JB009181

D'Auria, L., Martini, M., Esposito, A., Ricciolino, P., & Giudicepietro, F. (2008). A unified 3D velocity model for the Neapolitan volcanic areas. In W. Marzocchi, & A. Zollo (Eds.), *Conception, verification and application of innovative techniques to study active volcanoes*, (pp. 375–390). Italy: INGV-DPC, Napoli. http://hdl.handle.net/2122/8688

D'Auria, L., Pepe, S., Castaldo, R., Giudicepietro, F., Macedonio, G., Ricciolino, P., et al. (2015). Magma injection beneath the urban area of Naples: A new mechanism for the 2012–2013 volcanic unrest at Campi Flegrei caldera. *Scientific Reports*, *5*, 13100. https://doi.org/10.1038/srep13100

De Martino, P., Tammaro, U., & Obrizzo, F. (2014). GPS time series at Campi Flegrei caldera (2000–2013). *Annals of Geophysics*, *57*(2), S0213. https://doi.org/10.4401/ag-6431

De Natale, G., Troise, C., Pingue, F., Mastrolorenzo, G., Pappalardo, L., Battaglia, M., & Boschi, E. (2006). The Campi Flegrei caldera: Unrest mechanisms and hazards. In C. Troise, G. De Natale, & C. R. J. Kilburn (Eds.), *Mechanisms of activity and unrest at large calderas*, (Vol. 269, pp. 25–45). London: Geological Society, Special Publications.

De Vivo, B., Rolandi, G., Gans, P. B., Calvert, A., Bohrson, W. A., Spera, F. J., & Belkin, H. E. (2001). New constraints on the pyroclastic eruptive history of the Campanian volcanic Plain (Italy). *Mineralogy and Petrology*, *73*(1-3), 47–65. https://doi.org/10.1007/s007100170010

Deino, A. L., Orsi, G., de Vita, S., & Piochi, M. (2004). The age of the Neapolitan Yellow Tuff caldera-forming eruption (Campi Flegrei caldera – Italy) assessed by 40Ar/39Ar dating method. *Journal of Volcanology and Geothermal Research*, *133*(1–4), 157–170. https://doi.org/10.1016/S0377-0273(03)00396-2

Del Gaudio, C., Aquino, I., Ricciardi, G. P., Ricco, C., & Scandone, R. (2010). Unrest episodes at Campi Flegrei: A reconstruction of vertical ground movements during 1905–2009. *Journal of Volcanology and Geothermal Research*, *195*(1), 48–56. https://doi.org/10.1016/j.jvolgeores.2010.05.014

Di Renzo, V., Arienzo, I., Civetta, L., D'Antonio, M., Tonarini, S., Di Vito, M. A., & Orsi, G. (2011). The magmatic feeding system of the Campi Flegrei caldera: Architecture and temporal evolution. *Chemical Geology*, *281*(3-4), 227–241. https://doi.org/10.1016/j.chemgeo.2010.12.010

Fournier, N., & Chardot, L. (2012). Understanding volcano hydrothermal unrest from geodetic observations: Insights from numerical modeling and application to White Island volcano, New Zealand. *Journal of Geophysical Research*, *117*, B11208. https://doi.org/10.1029/2012JB009469

Hurwitz, S., Christansen, L. B., & Hsieh, P. E. (2007). Hydrothermal fluid flow and deformation in large calderas: Inferences from numerical simu- lations. *Journal of Geophysical Research*, *112*, B02206. https://doi.org/10.1029/2006JB004689

Hutnak, M., Hurwitz, S., Ingebritsen, S. E., & Hsieh, P. A. (2009). Numerical models of caldera deformation: Effects of multiphase and multicomponent hydrothermal fluid flow. *Journal of Geophysical Research*, *114*, B04411. https://doi.org/10.1029/2008JB006151

Lanari, R., Berardino, P., Fornaro, G., Guarino, S., Sansosti, E., Borgström, S., et al. (2004). The use of IFSAR and classical geodetic techniques for caldera unrest episodes: Application to the Campi Flegrei uplift event of 2000. *Journal of Volcanology and Geothermal Research*, *133*(1–4), 247–260. https://doi.org/10.1016/S0377-0273(03)00401-3

Lawson, C. L., & Hanson, R. J. (1974). *Solving least squares problems* (chap. 23, 161 pp.). Prentice-Hall.

Morhange, C., Marriner, N., Laborel, J., Todesco, M., & Oberlin, C. (2006). Rapid Sea-level movements and noneruptive crustal deformations in the Phlegrean fields caldera, Italy. *Geology*, *34*(2), 93–96. https://doi.org/10.1130/G21894

Moridis, G., & Pruess, K. (1998). Flow and transport simulations using T2CG1. A package of conjugate gradient solvers for the TOUGH2 family of codes. Lawrence Berkeley Nat. Lab. Report LBL 36235.

Orsi, G., Civetta, L., D'Antonio, M., Di Girolamo, P., & Piochi, M. (1995). Step-filling and development of a three-layer magma chamber: The Neapolitan Yellow Tu¡ case history. *Journal of Volcanology and Geothermal Research*, *67*(4), 291–312. https://doi.org/10.1016/0377-0273(94)00119-2

Orsi, G., Civetta, L., Del Gaudio, C., De Vita, S., Di Vito, M. A., Isaia, R., et al. (1999). Short-term ground deformations and seismicity in the nested Campi Flegrei caldera (Italy). *Journal of Volcanology and Geothermal Research*, *91*(2-4), 415–451. https://doi.org/10.1016/S0377-0273(99)00050-5

Orsi, G., Di Vito, M. A., & Isaia, R. (2004). Volcanic hazard assessment at the restless Campi Flegrei caldera. *Bulletin of Volcanology*, *66*(6), 514–530. https://doi.org/10.1007/s00445-003-0336-4

Orsi, G., di Vito, M. A., Selva, J., & Marzocchi, W. (2009). Longterm forecast of eruption style and size at Campi Flegrei caldera (Italy). *Earth and Planetary Science Letters*, *287*(1-2), 265–276. https://doi.org/10.1016/j.epsl.2009.08.013

Pappalardo, L., Civetta, L., D'Antonio, M., Deino, A. L., Di Vito, M. A., Orsi, G., et al. (1999). Chemical and isotopical evolution of the Phlegrean magmatic system before the Campanian Ignimbrite (37 ka) and the Neapolitan Yellow Tuff (12 ka) eruptions. *Journal of Volcanology and Geothermal Research*, *91*(2-4), 141–166. https://doi.org/10.1016/S0377-0273(99)00033-5

Parascandola, A. (1947). *I Fenomeni Bradisismici del Serapeo di Pozzuoli*. Naples: Privately published.

Petrillo, Z., Chiodini, G., Mangiacapra, A., Caliro, S., Capuano, P., Russo, G., Cardellini, C., et al. (2013). Defining a 3D physical model for the hydrothermal circulation at Campi Flegrei caldera (Italy). *Journal of Volcanology and Geothermal Research*, *264*, 172–182. ISSN 0377-0273. https://doi.org/10.1016/j.jvolgeores.2013.08.008

Pruess, K. (1987). TOUGH user's guide. Lawrence Berkeley Lab. Report LBL 20700.

Pruess, K. (1991). TOUGH2—A general purpose numerical simulator for multiphase fluid and heat flow. L. B. L. Report. LBL, Berkeley, CA, p. 29400.

Pruess, K. (2004). The TOUGH codes—A family of simulation tools for multiphase flow and transport processes in permeable media. *Vadose Zone Journal*, *3*, 738–746. https://doi.org/10.2113/3.3.738

Rinaldi, A. P., Todesco, M., & Bonafede, M. (2010). Hydrothermal instability and ground displacement at the Campi Flegrei caldera. *Physics of the Earth and Planetary Interiors*, *178*(3–4), 155–161. https://doi.org/10.1016/j.pepi.2009.09.005

Rosi, M., & Sbrana, A. (1987). Phlegrean fields. Quaderni de "La Ricerca Scientifica" Cons. Naz. delle Ric., Rome.

Sutton, F. M., & Mc Nubb, A. (1977). Boiling curves at Broad-lands Field, New Zealand. *New Zealand Journal of Science*, *20*, 333–337.

Todesco, M. (2009). Signals from the Campi Flegrei hydrothermal system: Role of a "magmatic" source of fluids. *Journal of Geophysical Research*, *114*, B05201. https://doi.org/10.1029/2008JB006134

Todesco, M., & Berrino, G. (2005). Modeling hydrothermal fluid circulation and gravity signals at the Phlegraean Fields caldera. *Earth and Planetary Science Letters*, *240*, 328–338. https://doi.org/10.1016/j.epsl.2005.09.016

Todesco, M., Chiodini, G., & Macedonio, G. (2003). Monitoring and modeling hydrothermal fluid emission at La Solfatara (Phlegrean Fields, Italy). An interdisciplinary approach to the study of diffuse degassing. *Journal of Volcanology and Geothermal Research*, *125*(1-2), 57–79. https://doi.org/10.1016/S0377-0273(03)00089-1

Todesco, M., Rinaldi, A. P., & Bonafede, M. (2010). Modeling of unrest signals in heterogeneous hydrothermal systems. *Journal of Geophysical Research*, *115*, B09213. https://doi.org/10.1029/2010JB007474

Todesco, M., Rutqvist, J., Chiodini, G., Pruess, K., & Oldenburg, C. M. (2004). Modeling of recent volcanic episodes at Phlegrean Fields (Italy): Geochemical variations and ground deformation. *Geothermics*, *33*(4), 531–547. https://doi.org/10.1016/j.geothermics.2003.08.014

Trasatti, E., & Bonafede, M. (2008). Gravity changes due to overpressure sources in 3D heterogeneous media: Application to Campi Flegrei caldera, Italy. *Annals of Geophysics*, *51*, 121–135.

Trasatti, E., Polcari, M., Bonafede, M., & Stramondo, S. (2015). Geodetic constraints to the source mechanism of the 2011–2013 unrest at Campi Flegrei (Italy) caldera. *Geophysical Research Letters*, *42*, 3847–3854. https://doi.org/10.1002/2015GL063621

Vasco, D. W., Wicks, C., & Karasaki, K. (2002). Geodetic imaging: High resolution reservoir monitoring using satellite interferometry. *Geophysical Journal International*, *149*, 555–571.

Zollo, A., Maercklin, N., Vassallo, M., Dello Iacono, D., Virieux, J., & Gasparini, P. (2008). Seismic reflections reveal a massive melt layer feeding Campi Flegrei caldera. *Geophysical Research Letters*, *35*, L12306. https://doi.org/10.1029/2008GL034242